

Improving Full Waveform Inversion in Large Model Era

Yinan Feng

School of Data Science and Society
University of North Carolina at Chapel Hill
Chapel Hill, NC, USA
ynf@unc.edu

Peng Jin

The Pennsylvania State University
State College, PA, USA
pqj5125@psu.edu

Yuzhe Guo

School of Data Science and Society
University of North Carolina at Chapel Hill
Chapel Hill, NC, USA
guoyuz@unc.edu

Yinpeng Chen

Google DeepMind
yinpengc@google.com

Youzuo Lin

School of Data Science and Society
University of North Carolina at Chapel Hill
Chapel Hill, NC, USA
yzlin@unc.edu

Abstract

Full Waveform Inversion (FWI) is a highly nonlinear and ill-posed problem that aims to recover subsurface velocity maps from surface-recorded seismic waveforms data. Existing data-driven FWI typically uses small models, as available datasets have limited volume, geological diversity, and spatial extent, leading to substantial concerns about overfitting. Although they perform well on synthetic datasets, current methods fail to generalize to more realistic geological structures. In this work, we show that a model trained entirely on simulated and relatively simple data can generalize remarkably well to challenging and unseen geological benchmarks. We provide a working recipe that tames a billion-parameter model for FWI through coordinated scaling across three axes: model capacity, data diversity, and training strategy. Our model achieves state-of-the-art performance on OpenFWI and significantly narrows the generalization gap in data-driven FWI. Across six challenging geophysical benchmarks, including Marmousi, 2D SEG/EAGE Salt and Overthrust, 2004 BP, Sigsbee, and SEAM Phase I, it infers complex structures absent from the training set and delivers significant performance improvements (SSIM from 0.5844 to 0.7669). Overall, our results

demonstrate that with an appropriate scaling strategy, large models trained on simple synthetic data can achieve substantial generalization to more complex and realistic geological structures.

1. Introduction

Subsurface imaging is critical in scientific and industrial applications, including earthquake monitoring [32, 34], greenhouse gas storage [20, 37], medical imaging [14, 23], and oil and gas exploration [33, 36]. At its core, Full Waveform Inversion (FWI) serves as a representative method, which aims to reconstruct subsurface velocity maps from seismic data recorded on the surface, governed by the acoustic wave equation:

$$\frac{\partial^2 p(x, z, t)}{\partial t^2} = v^2(x, z) \nabla^2 p(x, z, t) + f(x, z, t), \quad (1)$$

where $p(x, z, t)$ is the pressure wavefield at spatial location (x, z) and time t , $v(x, z)$ is the 2D vertical velocity map, ∇^2 is the Laplacian operator, and $s(x, z, t)$ is the source term. In practice, seismic data are often the waveform data collected at the surface (i.e., $p(x, z = 0, t)$). While FWI

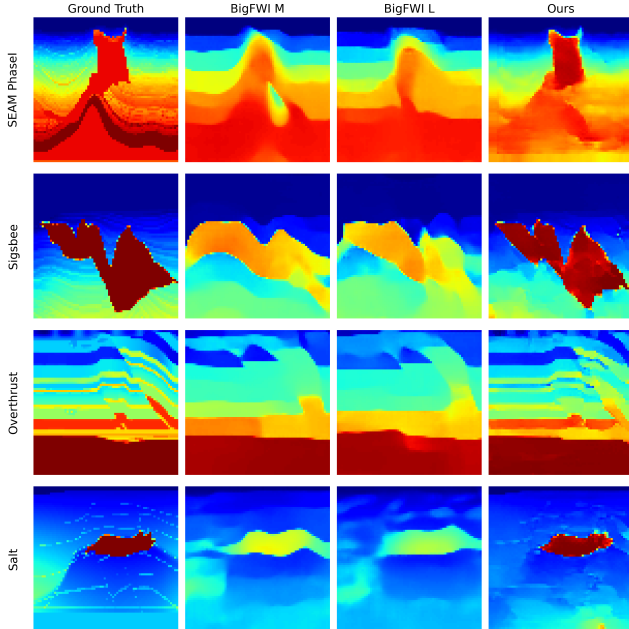


Figure 1. Reconstruction results on challenging realistic benchmarks. BigFWI tends to collapse toward over-smoothed, mean-shaped solutions that miss key interfaces and salt bodies. In contrast, our model produces sharper boundaries and geologically meaningful structures.

has the potential to produce high-resolution velocity maps, the inverse problem itself is inherently non-linear and ill-posed. In addition, the traditional iterative solvers based on gradient descent or adjoint-state methods are computationally demanding and sensitive to initialization, noise, and local minima [13, 25, 33]. These challenges have motivated growing interest in data-driven deep learning methods.

Recent advances in data-driven FWI have demonstrated the potential of deep neural networks to directly infer velocity maps from seismic data [3, 11, 18, 21, 38, 43]. However, these models typically operate at small to medium model scales. This is largely due to the limited scale of existing FWI datasets in terms of data volume, geological diversity, and spatial extent, which raises strong concerns about overfitting. Prior studies also report that modest increases in model size do not reliably improve performance [19]. Although current approaches achieve promising results on synthetic datasets, they struggle to generalize to more realistic geological structures, particularly those containing complex features such as salt bodies or strong heterogeneity. As illustrated in the second and third columns of Fig. 1, a state-of-the-art end-to-end method, BigFWI [19], often collapses into overly smoothed, mean-shaped solutions that fail to recover key interfaces or salt bodies, resulting in reconstructions that lack meaningful geological structure.

In this work, we show that a large model trained entirely on simulated and relatively simple data can generalize re-

markably well to challenging and unseen geological benchmarks. However, deploying large models for a scientific inverse problem is far from straightforward. Several fundamental questions arise. First, which architectural design can best capture seismic–velocity relationships, where accuracy and physical consistency are essential? Second, how can one mitigate data scarcity when existing datasets are orders of magnitude smaller than what large models typically require? Third, what learning strategies can effectively align the network with the underlying physical dependencies of wave propagation? Finally, how can post-processing be leveraged to enhance physical consistency and further improve reconstruction accuracy? We address these challenges by introducing a working recipe that tames a billion-parameter model for FWI through coordinated scaling across three axes: model capacity, data diversity, and training strategy. As illustrated in the rightmost column of Fig. 1, our method delivers significantly better reconstructions, recovering sharper layer boundaries and geologically meaningful high-velocity regions that prior methods fail to capture.

At the model level, our framework employs a one-billion-parameter transformer backbone that enables global contextual modeling between seismic and velocity tokens. Rather than relying on causal next-token generation, we adopt *non-causal parallel decoding*, allowing all velocity tokens to be generated simultaneously with full self-attention, significantly improving efficiency and accuracy. Complementing this backbone, we employ a ViT-VQGAN tokenizer [40] with an expanded bottleneck width that preserves fine geological details, avoiding the excessive information compression common in conventional VQGANs. The wide latent space is particularly well-suited for scientific inversion tasks where spatial fidelity is critical.

To address data scarcity, we train a latent diffusion model [27] on the OPENFWI dataset [9] to synthesize additional velocity maps. Each generated sample is paired with forward-simulated seismic data, ensuring physical consistency between the two modalities. This process expands the training corpus from 408k to over five million velocity–seismic pairs and introduces hybrid geological structures that mix heterogeneous features across sub-datasets. By substantially increasing both the quantity and structural diversity of training data, this diffusion-driven augmentation effectively meets the data requirements of the large transformer without relying on any real or realistic geological models.

In terms of learning strategies, we adopt a two-stage training pipeline. In the *supervised pre-training* stage, the model learns token-wise mappings from seismic-conditioned inputs to velocity representations. In the *RL-based post-training* stage, we further enhance model robustness through reinforcement learning (RL) optimiza-

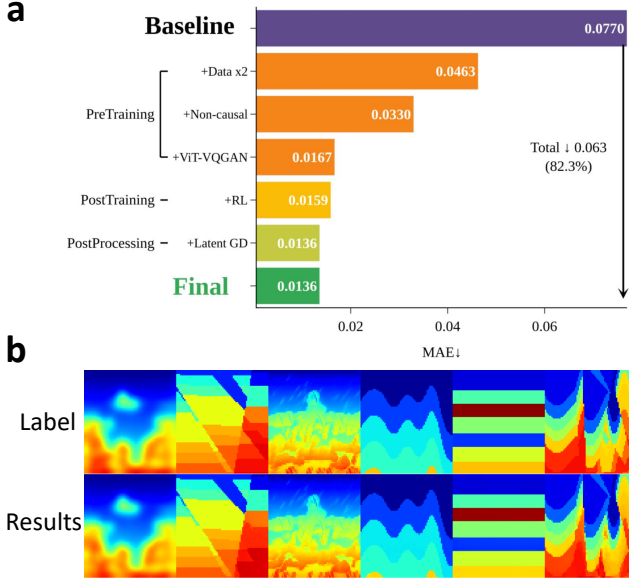


Figure 2. Overview of progressive model enhancements and final reconstruction quality. (a) Step-wise performance improvement as each component is introduced—from baseline to data augmentation, non-causal modeling, ViT VQGAN (without bottleneck), reinforcement learning alignment, and latent gradient refinement. (b) Illustration of the final reconstruction results, showing sharp structures and fine geological details across diverse scenarios.

tion [29, 44]. We formulate velocity token generation as a discrete policy optimization problem, and utilize map-level rewards that encourage geological continuity and physical plausibility, enabling the model to move beyond the limitations of purely supervised learning.

In the post-processing stage, we first perform a physics-based gradient descent (GD) refinement to improve the physical consistency of the predicted velocity maps. This step optimizes the continuous latent embeddings in the VQGAN decoder with respect to forward-modeling residuals, enforcing consistency with the governing wave equation. To further mitigate the ill-posedness of FWI, we additionally employ stochastic sampling and ensemble aggregation to combine multiple reconstructions when evaluating on realistic and unseen datasets, thereby reducing ambiguity and reducing predictive uncertainty.

Through extensive experiments, we demonstrate that each component of our large-model recipe contributes to improved performance and stability. Figure 2 summarizes the progressive gains and final reconstruction quality on OPENFWI achieved by different components of our framework. Overall, our approach achieves state-of-the-art results on the synthetic OPENFWI benchmark and, more importantly, substantially narrows the long-standing generalization gap on realistic geophysical datasets, including Marmousi, 2D SEG/EAGE Salt and Overthrust, 2004 BP, Sigsbee, and SEAM Phase I.

2. Methodology

In this section, we outline the trajectory from a baseline toward a modern large-model FWI system based on discrete sequence modeling. Figure 2 summarizes the step-wise performance improvements contributed by each component and presents the final reconstruction results. Our roadmap is as follows. We begin with an autoregressive baseline using two tokenization schemes, and then progressively introduce a sequence of design decisions: (1) data scaling and augmentation, (2) a non-causal transformer for parallel token prediction, (3) a ViT-VQGAN tokenizer without a compression bottleneck, and post-training modules including (4) policy optimization with velocity-level rewards (RL), and (5) latent-space gradient refinement. Together, these components yield state-of-the-art reconstruction accuracy and strong generalization ability.

2.1. Baseline: Auto-regression Model

Task formulation. Given seismic data $\mathbf{s} \in \mathbb{R}^{N_s \times T \times R}$, where N_s , T , and R denote the number of sources, temporal steps, and receivers, respectively, and its corresponding ground-truth velocity map $\mathbf{v} \in \mathbb{R}^{H \times W}$, the goal of the backbone model is to predict the discretized velocity token sequence $\mathbf{y} = (y_1, \dots, y_{L_v})$ whose indices correspond to entries in a pretrained VQGAN codebook. The conditional generation process follows an autoregressive formulation:

$$p_\theta(\mathbf{y} | \mathbf{s}) = \prod_{i=1}^{L_v} p_\theta(y_i | \mathbf{s}, y_{<i}), \quad (2)$$

where θ are backbone model parameters. During inference, the predicted sequence \mathbf{y} is decoded by the VQGAN decoder to reconstruct the full-resolution velocity map $\hat{\mathbf{v}}$.

The auto-regressive baseline comprises the following pipeline: (1) seismic data are tokenized via patch embedding; (2) velocity maps are quantized by a frozen VQGAN encoder; (3) both are concatenated into a unified token sequence; (4) a causal transformer predicts velocity tokens autoregressively; and (5) predicted tokens are decoded into inversion result $\hat{\mathbf{v}}$.

Tokenization. The model employs two independent tokenizers that embed seismic and velocity data into their corresponding token spaces.

(a) **Seismic tokenizer.** The seismic data is first divided into spatio-temporal patches and projected through a linear embedding layer (`PatchEmbed`) to form a continuous token sequence $\mathbf{m} \in \mathbb{R}^{L_s \times C_h}$. A positional encoding $\mathbf{E}_{\text{pos}}^{(s)}$ is added to preserve ordering:

$$\mathbf{m} = \text{PatchEmbed}(\mathbf{s}) + \mathbf{E}_{\text{pos}}^{(s)}. \quad (3)$$

(b) Velocity tokenizer. A pretrained VQGAN encoder discretizes the velocity map \mathbf{v} into a latent grid and quantizes it into codebook tokens. Each latent feature is linearly projected to match the backbone model’s hidden dimension and combined with positional embeddings:

$$\mathbf{t} = \text{Linear}(\text{Enc}(\mathbf{v})) + \mathbf{E}_{\text{pos}}^{(v)}. \quad (4)$$

While the linear projection is trained together with the large transformer model, the VQGAN tokenizer remains frozen to ensure a consistent latent representation capturing fine geological structure.

Input Sequence construction. We concatenate the seismic and velocity embeddings into a single multimodal “visual sentence”:

$$[\text{BOS}, \langle B_{\text{seis}} \rangle, \mathbf{m}, \langle E_{\text{seis}} \rangle, \langle D_{\text{id}} \rangle, \langle B_{\text{vel}} \rangle, \mathbf{t}], \quad (5)$$

where special tokens BOS marks the beginning of the sequence; $\langle B_{\text{seis}} \rangle$ and $\langle E_{\text{seis}} \rangle$ delimit the start and end of the seismic token segment \mathbf{m} ; $\langle D_{\text{id}} \rangle$ is an auxiliary task-specific identifier token that is trained to encode the inversion objective or dataset identity to help model learning; $\langle B_{\text{vel}} \rangle$ denotes the beginning of the velocity segment; and \mathbf{t} represents the ground-truth velocity tokens from the VQGAN tokenizer.

Network backbone and causal decoding. The backbone is a causal transformer with 1B parameters. During training, only the velocity positions are supervised with the standard token-level cross-entropy loss, while all preceding tokens serve as conditioning context. In inference, the transformer generates velocity tokens sequentially:

$$y'_i = \arg \max_y p_\theta(y | \mathbf{s}, y_{<i}), \quad i = 1, \dots, L_v. \quad (6)$$

The completed sequence \mathbf{y}' is then decoded through the VQGAN’s decoder to produce $\hat{\mathbf{v}}$:

$$\hat{\mathbf{v}} = \text{Dec}(\mathbf{y}'). \quad (7)$$

While this formulation enables explicit sequence modeling of seismic-velocity relations, it enforces strictly sequential decoding, limiting global token interaction and computational efficiency. These limitations motivate the transition to non-causal, parallel predictions.

2.2. Macro Design

Data Augmentation. To enhance data diversity and mitigate overfitting, we construct a large-scale synthetic dataset through a two-stage generation pipeline. First, a latent diffusion model is trained in the velocity domain to synthesize subsurface structures, enabling sampling of geologically diverse velocity maps. Second, for each synthesized velocity

map $\hat{\mathbf{v}}$, an acoustic forward simulator generates the corresponding seismic observation $\tilde{\mathbf{s}} = f(\hat{\mathbf{v}})$, ensuring physical consistency between the two modalities. This process enlarges the training corpus by approximately tenfold beyond the available paired samples, encompassing a wider range of geophysical conditions and acquisition geometries, which introduces more diverse synthetic cases that mix heterogeneous geological features from different subdatasets in the original dataset.

Non-Causal Sequence Modeling. While the baseline autoregressive transformer predicts velocity tokens sequentially, we reformulate inversion as a *non-causal, parallel prediction* problem to exploit bidirectional context fully. The model operates on a unified input sequence constructed as

$$[\text{BOS}, \langle B_{\text{seis}} \rangle, \mathbf{m}, \langle E_{\text{seis}} \rangle, \langle D_{\text{id}} \rangle, \langle B_{\text{vel}} \rangle, \mathbf{p}_{\text{vel}}], \quad (8)$$

where \mathbf{p}_{vel} denotes learnable placeholder tokens corresponding to velocity-token positions. These placeholders are optimized jointly with the transformer to represent the output embedding space. Unlike causal decoding, all velocity tokens are generated simultaneously, with the attention mask set to permit full self-attention across seismic and velocity segments. This non-causal formulation enables global token interaction, improving both efficiency and reconstruction accuracy.

ViT-VQGAN Tokenizer. To obtain discrete and high-fidelity representations of velocity maps, we replace the original pretrained VQGAN with a ViT-based architecture [40]. Unlike the previous architecture, this variant removes the compression bottleneck by interpolating the input and output to a resolution five times larger, enabling the preservation of fine-scale geological structure. Rotary positional embeddings (RoPE) [31] are applied within attention layers to maintain spatial coherence. This tokenizer achieves substantially lower reconstruction error with a smaller network, providing an effective discrete representation space for large-scale sequence modeling.

2.3. Post-Training Enhancements

The macro design establishes a scalable sequence-modeling framework for FWI. To further enhance physical fidelity and convergence, we introduce two complementary post-training strategies that strengthen the model from different perspectives: a reinforcement learning (RL) stage that aligns model outputs with velocity-level rewards, and a latent-space gradient refinement mechanism that corrects residual artifacts in the decoder’s continuous representation. Each stage builds upon the trained model without retraining the tokenizer, progressively improving the reconstruction quality and physical consistency.

Policy Optimization with Velocity-Level Rewards. To further align model outputs with high-level structural fidelity, we employ a reinforcement-learning-style fine-tuning procedure that treats the trained transformer as a stochastic policy $\pi_\theta(\mathbf{y} \mid \mathbf{s}) = \prod_{i=1}^{L_v} p_\theta(y_i \mid \mathbf{s})$. Velocity tokens are sampled independently across spatial positions. The policy is optimized to maximize the expected reward associated with the generated velocity map:

$$\max_{\theta} \mathbb{E}_{\mathbf{y} \sim \pi_\theta(\cdot \mid \mathbf{s})} [-\|\mathbf{v} - \hat{\mathbf{v}}(\mathbf{y})\|]. \quad (9)$$

Then a GRPO-style optimization [44] was applied. This contrasts with purely supervised cross-entropy training and encourages the model to generate token sequences that are holistically better at the map level, rather than merely correct on a per-token basis. The RL stage further reweights the model’s token predictions to prefer sequences that produce geologically consistent velocity fields, serving as an improvement mechanism that bridges supervised objectives with structural priors.

Latent-Space Gradient Refinement. Finally, we perform gradient descent (GD) refinement directly in the decoder’s latent space to correct residual local inconsistencies after token prediction. Let \mathbf{z} denote the continuous latent features produced by the VQGAN encoder prior to quantization, and let \mathbf{z}_{pred} be the latent reconstructed from the predicted tokens. Instead of updating the velocity map $\hat{\mathbf{v}}$ itself, as is done in traditional gradient-based FWI, we refine \mathbf{z}_{pred} by optimizing a differentiable reconstruction objective:

$$\mathbf{z}_{k+1} = \mathbf{z}_k - \eta \nabla_{\mathbf{z}} \mathcal{L}_{\text{rec}}(\mathcal{F}(\text{Dec}(\mathbf{z}_k)), \mathbf{s}), \quad (10)$$

where η is the learning rate and \mathcal{L}_{rec} is a reconstruction loss on seismic data. Because gradients are computed with respect to \mathbf{z} rather than $\hat{\mathbf{v}}$, this refinement operates in a smooth latent manifold. This design differs from traditional FWI, which directly updates the velocity map and therefore requires strong regularization to avoid unstable or physically implausible solutions. By refining in the latent space of the VQGAN, the model retains high-frequency geological details while improving global consistency, resulting in improved accuracy.

3. Experiments

In this section, we systematically evaluate the proposed large-model FWI framework. We begin by describing the experimental setup, including datasets, preprocessing, and training configurations. We then present quantitative and qualitative results, followed by a comparison of two VQGAN tokenizers and an assessment of the effectiveness of reinforcement learning. Finally, we examine the model’s performance on more realistic and previously unseen geological data, demonstrating its ability to generalize far beyond the training distribution.

3.1. Dataset and Training Setup

In the experiments, we evaluate the performance of our model using the OPENFWI dataset [9], a comprehensive benchmark collection comprising 11 2D subsets of realistic synthetic seismic data paired with subsurface velocity maps, designed explicitly for FWI tasks. These subsets represent diverse geological structures, including curved velocity layers, flat velocity layers, and flat layers intersected by faults. Our experiments utilized 10 subsets (Fault, Vel, and Style Families) with the same resolution to ensure a thorough assessment. There are a total of 408K training samples. For additional details, we refer readers to the original OpenFWI paper [9].

Data Augmentation. To increase data diversity and meet the scale required by large-model training, we employ a generative augmentation strategy based on a latent diffusion model [27] trained on the OPENFWI training set. After training, synthetic velocity maps are sampled from the learned latent distribution, and each map is paired with its corresponding seismic data generated via the acoustic forward modeling operator. The synthesized samples achieve a Fréchet Inception Distance (FID) of 260.33 when evaluated against the original OPENFWI dataset. This process expands the number of training pairs from 408,000 to approximately 5 million, significantly improving data coverage and supporting large-scale model training.

Training Configuration. The VQGANs and latent diffusion model are trained on NVIDIA H100 GPUs, while the transformer backbone is trained on four NVIDIA L40 GPUs with a batch size of 8. We use the AdamW optimizer with a learning rate of $5e-4$, weight decay of $5e-2$, and a cosine learning rate schedule with a 10-epoch warmup. Training spans 100 epochs for the base models and 700K iterations for reinforcement-learning fine-tuning. All predicted velocity maps are evaluated using MAE under the normalized range $[-1, 1]$, consistent with prior work [9, 12, 38].

3.2. Comparison with Baseline Methods.

Table 1 reports the quantitative comparison between our model variants and the CNN-based BigFWI baselines [19]. Across all settings, our framework significantly outperforms prior methods and demonstrates clear benefits from scaling data, architecture, and training strategy.

The causal baseline achieves only moderate accuracy (MAE 0.0770). Due to the large model size and the limited scale of the OPENFWI training set, this causal baseline cannot operate at its full capacity, leading to suboptimal performance. Increasing the training data by a factor of two reduces the error to 0.0463, matching the performance range of BigFWI. Scaling to ten times more data further improves

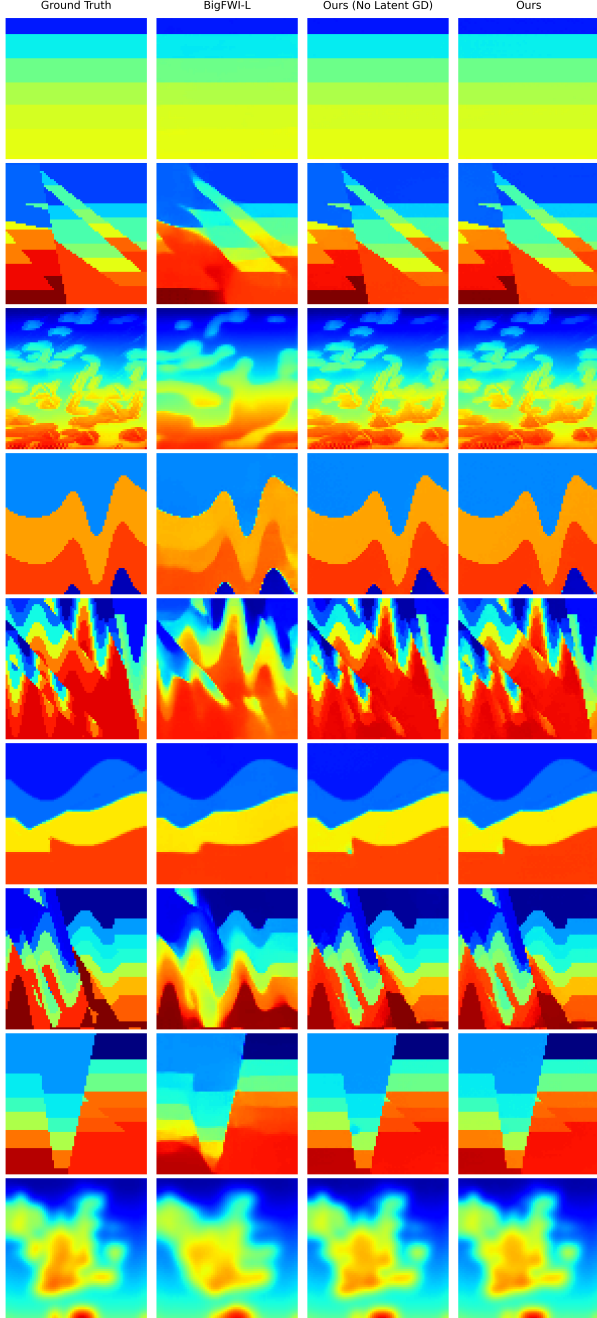


Figure 3. **Qualitative comparison** of reconstructed velocity maps.

accuracy to 0.0368, indicating strong data-driven scalability. Note that, unlike the other variants, this model with 10 times data is trained for only 20 epochs with a 1-epoch warmup.

Switching from causal to non-causal decoding yields a larger improvement, reducing the MAE from 0.0463 to 0.0330 (under the same training data level) by allowing full bidirectional attention among all tokens. Replacing the original U-Net VQGAN tokenizer with the ViT-VQGAN, which is trained on the full $\times 10$ augmented dataset, leads

Table 1. **Quantitative comparison with baseline methods.** Each model is organized incrementally, with each row cumulatively including components introduced in prior rows.

	Model	MAE \downarrow	#Parameters
	BigFWI-M [19]	0.0437	28M
	BigFWI-L [19]	0.0432	87M
Causal	Baseline	0.0770	1.09B
	+ Data $\times 2$	0.0463	1.09B
	+ Data $\times 10$	0.0368	1.09B
Non-Causal	Data $\times 2$	0.0330	1.09B
	+ ViT-VQGAN	0.0167	1.03B
	+ RL	0.0159	1.03B
	+ Latent GD	0.0136	1.03B

to a substantial improvement (MAE 0.0167). Notably, the backbone transformer for this final model is trained only on the $\times 2$ dataset. Reinforcement learning (RL) applied on top of the ViT-VQGAN version further reduces the error to 0.0159. Finally, applying physics-based latent gradient descent (GD) refinement yields the best performance (MAE 0.0136), establishing a new state of the art in data-driven FWI.

Remarkably, our model reaches state-of-the-art end-to-end performance for data-driven FWI, even before any post-processing refinement is applied. Overall, these results demonstrate that data scaling, non-causal modeling, improved tokenization, RL alignment, and physics-based refinement collectively define a powerful and extensible recipe for large-model FWI, pushing performance well beyond existing baselines.

Qualitative Results. Figure 3 shows representative reconstructions from BigFWI-L, our model without latent GD refinement, and our full model. BigFWI-L produces overly smooth velocity maps that miss key structural boundaries, whereas our end-to-end model (without GD) already recovers sharp interfaces, coherent stratigraphy, and realistic fault geometries across diverse geological scenarios.

The addition of latent GD refinement yields less visible changes, as seen in the comparison between the “Ours (No Latent GD)” and “Ours” columns. Thus, the primary role of GD to remove small high-frequency artifacts that are imperceptible to the human eye, such as layer-wise inconsistencies or localized oscillations introduced by the network. By enforcing physical consistency, GD refinement smooths out these physically implausible variations, improving numerical accuracy and physical correctness without significantly changing the visual appearance.

3.3. Zero-Shot Generalization on Realistic Geophysical Benchmarks

To evaluate generalization beyond the in-distributions synthetic data used during training, we evaluate our model

in a strict zero-shot setting on a collection of six widely used geophysical benchmark velocity models, including Marmousi [6], 2D SEG/EAGE Salt and Overthrust [2], 2004 BP [5], Sigsbee [24], and SEAM Phase I [10]. These datasets contain substantially more complex and heterogeneous geological structures than those seen in the OPENFWI training distribution. A prominent example is the presence of large salt bodies: high-velocity, sharply bounded formations that generate strong reflections and multipathing effects. Such structures create discontinuous wavefronts and non-convex inversion landscapes, making them uniquely challenging for FWI [33]. Their absence in the training data makes zero-shot reconstruction particularly difficult for data-driven approaches.

In particular, the Salt and Overthrust originate from 3D velocity volumes; we uniformly extract ten 2D slices from each volume. For SEAM Phase I, we only use the V_p as we use an acoustic forward modeling. All velocity maps are downsampled to 70×70 and linearly mapped to the range 1500–4500 m/s to match the normalization used during training. Seismic data are generated with the same acoustic forward-modeling operator as in OPENFWI: five evenly spaced sources with a 15 Hz Ricker wavelet, recorded by 70 receivers sampling 1,000 timesteps over one second.

For evaluation, our model predicts five samples for each velocity map using stochastic sampling. Each sample is refined through latent space gradient descent (GD), and the final prediction is obtained by averaging the refined outputs. We evaluate predicted velocity maps using MAE, RMSE, and Structural Similarity (SSIM). MAE and RMSE quantify pixel-wise errors, while SSIM captures perceptual similarity, reflecting the structured information of velocity maps where distortions can be easily perceived by a human. Note that MAE and MSE are computed in the range [1500, 4500], and SSIM in [0, 1].

Quantitative results are reported in Table 2. The results for the Salt and Overthrust datasets are averaged over ten uniformly sampled 2D slices extracted from their 3D volumes. Across all six benchmark families and 26 velocity maps, our method achieves the best overall performance, producing substantially lower error and much higher SSIM than the BigFWI baselines. For ablation, without latent GD refinement, the ensemble prediction reaches an MAE of 148.35, while incorporating GD further reduces the MAE to 139.81.

While BigFWI attains better MAE in a few individual cases (e.g., SEAM Phase I and Salt), the corresponding reconstructions are severely oversmoothed and lack interpretable geological structure. This is clearly visible in Figure 4, where BigFWI tends to collapse toward mean-shaped solutions that fail to recover key interfaces or high-contrast anomalies. In contrast, our model reconstructs coherent stratigraphy, sharper layer boundaries, and geologi-

cally meaningful high-velocity regions.

These differences are particularly pronounced for salt-body targets. Despite having large distribution shift, our model successfully delineates salt geometry and surrounding stratification, demonstrating strong generalization beyond the training distribution. Overall, the zero-shot results show that our large-model paradigm not only reduces numerical error but, more importantly, produces physically meaningful and interpretable reconstructions on challenging and previously unseen geological structures.

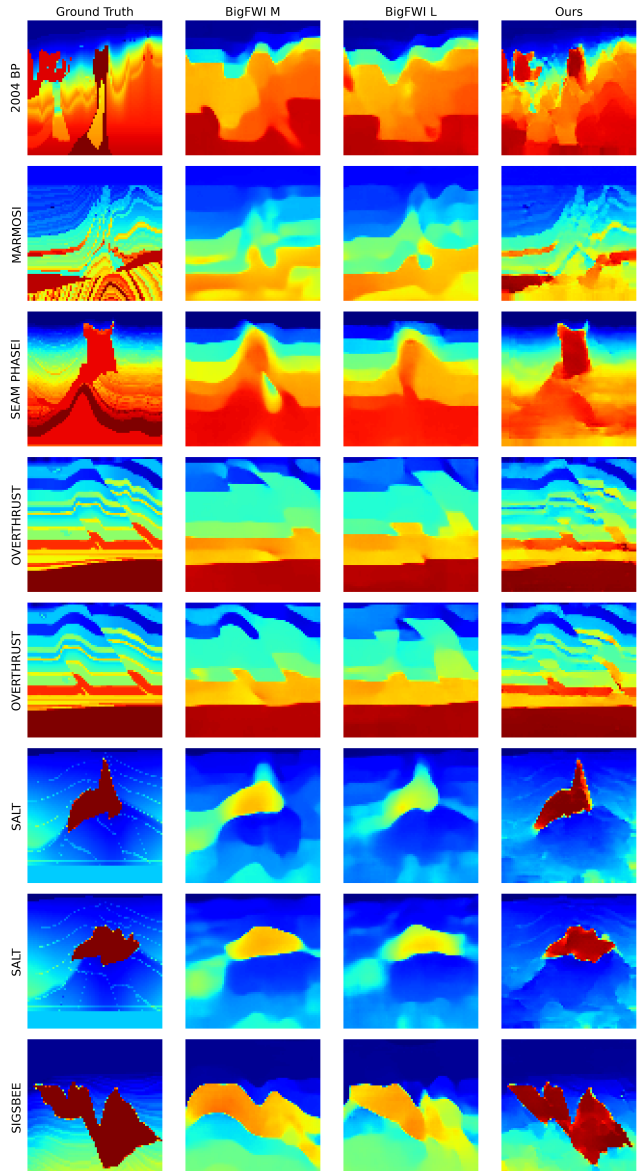


Figure 4. **Qualitative comparison of reconstructed velocity maps.** Our method produces sharper structures and finer structures across complex regions.

Table 2. **Quantitative performance across six benchmark families.** Our method achieves substantially lower MAE/RMSE and higher SSIM, with especially strong gains on SSIM.

Metrics	Model	Overall	2004 BP	Marmosi	SEAM Phase I	Overthrust	Salt	Sigsbee
MAE↓	BigFWI-M	199.20	247.15	226.63	185.02	221.57	150.13	431.60
	BigFWI-L	210.99	238.31	233.22	190.84	243.25	159.07	398.08
	Ours	139.81	133.45	145.62	199.44	118.25	155.22	148.40
RMSE↓	BigFWI-M	312.15	390.30	346.13	289.37	297.96	281.57	715.32
	BigFWI-L	327.79	377.88	349.42	294.67	320.46	301.74	656.29
	Ours	241.78	247.61	251.12	281.57	199.76	268.67	353.37
SSIM↑	BigFWI-M	0.5844	0.5828	0.5074	0.6371	0.5020	0.6691	0.5852
	BigFWI-L	0.5579	0.5962	0.4930	0.6425	0.4516	0.6554	0.5973
	Ours	0.7669	0.7560	0.7201	0.7804	0.7916	0.7425	0.8071

3.4. Effectiveness of Reinforcement Learning

To evaluate the effectiveness of reinforcement learning (RL), we apply RL to three representative base models with different configurations. The results are summarized in Table 3. RL consistently improves reconstruction accuracy across all settings.

For the causal transformer trained with doubled data (*Causal + Data, x2*), RL yields a substantial 25.7% reduction in MAE, demonstrating that policy optimization provides meaningful gains even under strictly autoregressive decoding. A similar, though smaller, improvement is observed for the non-causal model (*Non-Causal + Data, x2*), where RL reduces the MAE by 10.6%, indicating that RL remains beneficial even when the model already leverages full bidirectional context during decoding. RL also improves performance in our final ViT-VQGAN-enhanced model (*Non-Causal + Data, x2 + ViT-VQGAN*). Starting from an MAE of 0.0167, RL reduces the error to 0.0159, corresponding to a 4.7% improvement. As expected, the gains become smaller as the base model becomes stronger and harder to improve.

Overall, these results demonstrate that RL consistently yields measurable improvements in reconstruction fidelity across a broad range of model configurations.

Table 3. **Qualitative comparison of reinforcement learning** across different model configurations.

Model Configuration	MAE ↓
Causal + Data x2	0.0463
Causal + Data x2 + RL	0.0344
Non-Causal + Data x2	0.0330
Non-Causal + Data x2 + RL	0.0295
Non-Causal + Data x2 + ViT-VQGAN	0.0167
Non-Causal + Data x2 + ViT-VQGAN + RL	0.0159

3.5. Comparison of VQGAN Tokenizers

To evaluate reconstruction quality, we compare the conventional CNN-based VQGAN with the new ViT-based variant.

As shown in Table 4, the ViT-VQGAN achieves a markedly lower reconstruction error (MAE 0.0046) than the standard CNN-based VQGAN (MAE 0.0134), while using fewer parameters (43M vs. 104M). This improvement arises from replacing the convolutional encoder–decoder with a Vision Transformer (ViT) backbone and adopting a larger latent grid ($25 \times 25 \times 196$) without a compression bottleneck. The expanded latent representation preserves fine geological structures that are often lost when previous models heavily downsample the latent space. These results confirm that this new ViT-VQGAN tokenizer offers superior reconstruction fidelity, providing a more expressive and physically meaningful latent representation.

Table 4. **Quantitative comparison** of VQGANs.

Model	MAE ↓	Dim	#Parameters
VQGAN	0.0134	9x9x32	104M
ViT-VQGAN	0.0046	25x25x196	43M

4. Related Works

Recently, deep learning–based FWI methods have achieved notable performance improvements, ranging from purely data-driven approaches to those that incorporate computationally intensive forward operators for enhanced physical consistency [1, 22, 41]. Fully supervised approaches [3, 21, 38, 43] learn direct mappings from seismic data to velocity maps using paired datasets. Feng et al. [11, 12] decouple the seismic encoder and velocity decoder by leveraging latent-space correlations, enabling modular training. Siamese-FWI [28] adopts a Siamese architecture to align simulated and observed waveforms, facilitating cross-domain consistency. Unsupervised methods such as UPFWI [18] and Jia et al. [17] go further by removing the need for labels entirely. These approaches minimize waveform discrepancies under physical constraints using differentiable forward operators to optimize velocity predictions, though sacrificing accuracy and depending on computationally intensive solvers. Recently, diffusion models have emerged as an alternative, providing powerful generative priors that guide inverse recovery via plug-and-play (PnP) denois-

ing [8, 30, 42]. Wang et al. [35] demonstrate that such priors can improve FWI performance by regularizing the optimization landscape through learned data distributions.

Large language models (LLMs) have revolutionized natural language processing (NLP), achieving state-of-the-art performance across a broad range of tasks, from text generation [7, 16, 26] to complex reasoning and mathematical problem solving [15]. Motivated by this success, recent research has sought to extend LLM principles to perception and multimodal domains, giving rise to Large Vision Models (LVMs) that sequentialize visual inputs [4] and unified multimodal architectures such as MMaDA [39] that align reasoning across text and image modalities. Despite this rapid progress, scientific inverse problems, particularly those governed by physical processes such as wave propagation, remain underexplored within this paradigm.

5. Conclusion

We presented a large-model receipt for data-driven Full Waveform Inversion that combines a billion-parameter non-causal transformer, a high-fidelity ViT-VQGAN tokenizer trained on diffusion-augmented data, RL-based post-training, and physics-guided latent refinement. This framework achieves a significant performance improvement on OPENFWI and shows strong generalization to more realistic and previously unseen geological structures. Although demonstrated under simplified 2D acoustic settings, our results provide clear evidence that scaling model capacity, data diversity, and physics alignment is a promising direction for seismic inversion. We expect future extensions toward elastic and 3D physics, variable survey geometries, and higher-resolution domains to further advance the frontier of large-model geophysical imaging.

References

- [1] Amir Adler, Mauricio Araya-Polo, and Tomaso Poggio. Deep learning for seismic inverse problems: Toward the acceleration of geophysical analysis workflows. *IEEE Signal Processing Magazine*, 38:89–119, 2021. 8
- [2] Fred Aminzadeh. 3-d salt and overthrust seismic models. 1996. 7
- [3] Mauricio Araya-Polo, Joseph Jennings, Amir Adler, and Taylor Dahlke. Deep-learning tomography. *The Leading Edge*, 37(1):58–66, 2018. 2, 8
- [4] Yutong Bai, Xinyang Geng, Karttikeya Mangalam, Amir Bar, Alan L Yuille, Trevor Darrell, Jitendra Malik, and Alexei A Efros. Sequential modeling enables scalable learning for large vision models. In *Proceedings of the IEEE/CVF Conference on Computer Vision and Pattern Recognition*, pages 22861–22872, 2024. 9
- [5] FJ Billette and Sverre Brandsberg-Dahl. The 2004 bp velocity benchmark. In *67th EAGE Conference & Exhibition*, pages cp–1. European Association of Geoscientists & Engineers, 2005. 7
- [6] A Brougois, Marielle Bourget, Patriek Lailly, Michel Poulet, Patrice Ricarte, and Roelof Versteeg. Marmousi, model and data. In *EAGE workshop-practical aspects of seismic data inversion*, pages cp–108. European Association of Geoscientists & Engineers, 1990. 7
- [7] Tom Brown, Benjamin Mann, Nick Ryder, Melanie Subbiah, Jared D Kaplan, Prafulla Dhariwal, Arvind Neelakantan, Pranav Shyam, Girish Sastry, Amanda Askell, et al. Language models are few-shot learners. *Advances in neural information processing systems*, 33:1877–1901, 2020. 9
- [8] Hyungjin Chung, Jeongsol Kim, Michael T McCann, Marc L Klasky, and Jong Chul Ye. Diffusion posterior sampling for general noisy inverse problems. In *11th International Conference on Learning Representations, ICLR 2023*, 2023. 9
- [9] Chengyuan Deng, Shihang Feng, Hanchen Wang, Xitong Zhang, Peng Jin, Yanan Feng, Qili Zeng, Yinpeng Chen, and Youzuo Lin. Openfwi: Large-scale multi-structural benchmark datasets for full waveform inversion. *Advances in Neural Information Processing Systems*, 35:6007–6020, 2022. 2, 5
- [10] Michael Fehler and P Joseph Keliher. *SEAM phase 1: Challenges of subsalt imaging in tertiary basins, with emphasis on deepwater Gulf of Mexico*. Society of Exploration Geophysicists, 2011. 7
- [11] Yanan Feng, Yinpeng Chen, Shihang Feng, Peng Jin, Zicheng Liu, and Youzuo Lin. An intriguing property of geophysics inversion. In *International Conference on Machine Learning*, pages 6434–6446. PMLR, 2022. 2, 8
- [12] Yanan Feng, Yinpeng Chen, Peng Jin, Shihang Feng, and Youzuo Lin. Auto-linear phenomenon in subsurface imaging. In *Proceedings of the 41st International Conference on Machine Learning*. JMLR.org, 2024. 5, 8
- [13] Andreas Fichtner. *Full seismic waveform modelling and inversion*. Springer Science & Business Media, 2010. 2
- [14] Lluís Guasch, Oscar Calderón Agudo, Meng-Xing Tang, Parashkev Nachev, and Michael Warner. Full-waveform inversion imaging of the human brain. *NPJ digital medicine*, 3(1):28, 2020. 1
- [15] Daya Guo, Dejian Yang, Haowei Zhang, Junxiao Song, Ruoyu Zhang, Runxin Xu, Qihao Zhu, Shirong Ma, Peiyi Wang, Xiao Bi, et al. Deepseek-r1: Incentivizing reasoning capability in llms via reinforcement learning. *arXiv preprint arXiv:2501.12948*, 2025. 9
- [16] Aaron Jaech, Adam Kalai, Adam Lerer, Adam Richardson, Ahmed El-Kishky, Aiden Low, Alec Helyar, Aleksander Madry, Alex Beutel, Alex Carney, et al. Openai o1 system card. *arXiv preprint arXiv:2412.16720*, 2024. 9
- [17] Anqi Jia, Jian Sun, Bo Du, and Yuzhao Lin. Seismic full waveform inversion with uncertainty analysis using unsupervised variational deep learning. *IEEE Transactions on Geoscience and Remote Sensing*, 63:1–16, 2025. 8
- [18] Peng Jin, Xitong Zhang, Yinpeng Chen, Sharon Xiaolei Huang, Zicheng Liu, and Youzuo Lin. Unsupervised learning of full-waveform inversion: Connecting CNN and partial differential equation in a loop. In *Proceedings of the Tenth International Conference on Learning Representations (ICLR)*, 2022. 2, 8

- [19] Peng Jin, Yanan Feng, Shihang Feng, Hanchen Wang, Yinpeng Chen, Benjamin Consolvo, Zicheng Liu, and Youzuo Lin. An empirical study of large-scale data-driven full waveform inversion. *Scientific Reports*, 14(1):20034, 2024. 2, 5, 6
- [20] Dong Li, Suping Peng, Yinling Guo, Yongxu Lu, and Xiaoqin Cui. Co2 storage monitoring based on time-lapse seismic data via deep learning. *International Journal of Greenhouse Gas Control*, 108:103336, 2021. 1
- [21] Shucui Li, Bin Liu, Yuxiao Ren, Yangkang Chen, Senlin Yang, Yunhai Wang, and Peng Jiang. Deep-Learning Inversion of Seismic Data. *IEEE Transactions on Geoscience and Remote Sensing*, 58(3):2135–2149, 2020. 2, 8
- [22] Youzuo Lin, James Theiler, and Brendt Wohlberg. Physics-guided data-driven seismic inversion: Recent progress and future opportunities in full waveform inversion. *IEEE Signal Processing Magazine*, 40:115–133, 2023. 8
- [23] Luke Lozanski, Hanchen Wang, Fu Li, Mark Anastasio, Brendt Wohlberg, Youzuo Lin, and Umberto Villa. Learned full waveform inversion incorporating task information for ultrasound computed tomography. *IEEE Transactions on Computational Imaging*, 2024. 1
- [24] Josef Paffenholz, Bill McLain, Joerg Zasko, and P Joseph Keliher. Subsalt multiple attenuation and imaging: Observations from the sigsbee2b synthetic dataset. In *SEG international exposition and annual meeting*, pages SEG–2002. SEG, 2002. 7
- [25] R Gerhard Pratt. Seismic waveform inversion in the frequency domain, part 1: Theory and verification in a physical scale model. *Geophysics*, 64(3):888–901, 1999. 2
- [26] Alec Radford, Karthik Narasimhan, Tim Salimans, Ilya Sutskever, et al. Improving language understanding by generative pre-training. 2018. 9
- [27] Robin Rombach, Andreas Blattmann, Dominik Lorenz, Patrick Esser, and Björn Ommer. High-resolution image synthesis with latent diffusion models. In *Proceedings of the IEEE/CVF conference on computer vision and pattern recognition*, pages 10684–10695, 2022. 2, 5
- [28] Omar M. Saad, Randy Harsuko, and Tariq Alkhalifah. SiameseFWI: a deep learning network for enhanced full waveform inversion. *Journal of Geophysical Research: Machine Learning and Computation*, 1(3):e2024JH000227, 2024. 8
- [29] Zhihong Shao, Peiyi Wang, Qihao Zhu, Runxin Xu, Junxiao Song, Xiao Bi, Haowei Zhang, Mingchuan Zhang, YK Li, Yang Wu, et al. Deepseekmath: Pushing the limits of mathematical reasoning in open language models, 2024. 3
- [30] Yang Song, Liyue Shen, Lei Xing, and Stefano Ermon. Solving inverse problems in medical imaging with score-based generative models. In *International Conference on Learning Representations*, 2022. 9
- [31] Jianlin Su, Yu Lu, Shengfeng Pan, Bo Wen, and Yunfeng Liu. Roformer: Enhanced transformer with rotary position embedding, 2021. 4
- [32] Jeroen Tromp. Seismic wavefield imaging of earth’s interior across scales. *Nature Reviews Earth & Environment*, 1(1): 40–53, 2020. 1
- [33] Jean Virieux and Stéphane Operto. An overview of full-waveform inversion in exploration geophysics. *Geophysics*, 74(6):WCC1–WCC26, 2009. 1, 2, 7
- [34] Jean Virieux, Amir Asnaashari, Romain Brossier, Ludovic Métivier, Alessandra Ribodetti, and Wei Zhou. An introduction to full waveform inversion. In *Encyclopedia of exploration geophysics*, pages R1–1. Society of Exploration Geophysicists, 2017. 1
- [35] Fu Wang, Xinquan Huang, and Tariq Alkhalifah. A prior regularized full waveform inversion using generative diffusion models. *IEEE Transactions on Geoscience and Remote Sensing*, 61:1–11, 2023. 9
- [36] Hanchen Wang and Tariq Alkhalifah. Microseismic imaging using a source function independent full waveform inversion method. *Geophysical Journal International*, 214(1):46–57, 2018. 1
- [37] Hanchen Wang, Yinpeng Chen, Tariq Alkhalifah, Ting Chen, Youzuo Lin, and David Alumbaugh. Default: Deep-learning based fault delineation using the ibdp passive seismic data at the decatur co2 storage site. *arXiv preprint arXiv:2311.04361*, 2023. 1
- [38] Yue Wu and Youzuo Lin. Inversionnet: An efficient and accurate data-driven full waveform inversion. *IEEE Transactions on Computational Imaging*, 6:419–433, 2019. 2, 5, 8
- [39] Ling Yang, Ye Tian, Bowen Li, Xinchun Zhang, Ke Shen, Yunhai Tong, and Mengdi Wang. Mmada: Multimodal large diffusion language models. *arXiv preprint arXiv:2505.15809*, 2025. 9
- [40] Jiahui Yu, Xin Li, Jing Yu Koh, Han Zhang, Ruoming Pang, James Qin, Alexander Ku, Yuanzhong Xu, Jason Baldridge, and Yonghui Wu. Vector-quantized image modeling with improved vqgan. *arXiv preprint arXiv:2110.04627*, 2021. 2, 4
- [41] Xiwei Yu and Jianwei Ma. Deep learning for geophysics: Current and future trends. *Reviews of Geophysics*, 59: e2021RG000742, 2021. 8
- [42] Bingliang Zhang, Wenda Chu, Julius Berner, Chenlin Meng, Anima Anandkumar, and Yang Song. Improving diffusion inverse problem solving with decoupled noise annealing. In *Proceedings of the Computer Vision and Pattern Recognition Conference*, pages 20895–20905, 2025. 9
- [43] Zhongping Zhang, Yue Wu, Zheng Zhou, and Youzuo Lin. Velocitygan: Subsurface velocity image estimation using conditional adversarial networks. In *2019 IEEE Winter Conference on Applications of Computer Vision (WACV)*, pages 705–714. IEEE, 2019. 2, 8
- [44] Chujie Zheng, Shixuan Liu, Mingze Li, Xiong-Hui Chen, Bowen Yu, Chang Gao, Kai Dang, Yuqiong Liu, Rui Men, An Yang, et al. Group sequence policy optimization. *arXiv preprint arXiv:2507.18071*, 2025. 3, 5